Haynes, S.J., MacLeod, K.G., Ladant, J.B., Vande Guchte, A., Rostami, M.A., Poulsen, C.J., Martin, E.E.: *Geology*, doi:

LIST OF MATERIALS INCLUDED IN DATA REPOSITORY FILE

Bottom water temperature records in the Maastrichtian in the Pacific vs. the high-latitude South Atlantic and proto-Indian sectors of the Southern Ocean

Figure DR1. Compilation of benthic foraminiferal $\delta^{18}O$ from the Pacific, and South Atlantic and proto-Indian sectors of the Southern Ocean

Site locations and paleogeography

Figure DR2. Paleogeographic reconstruction for the Maastrichtian with all Pacific site locations (A), and a vertical profile of simulated water mass age across the Indonesian gateway in the Maastrichtian with 4× pre-industrial CO_2 concentrations (B).

Table DR1. Paleogeographic and bathymetric information

Sample processing and analytical methods

Table DR2. Neodymium isotopic data

Age models for DSDP Sites 289, 317, 463, and ODP Site 1186

Table DR3. Events used for each age model

Details of ocean climate model simulations

Table DR4. Water fluxes across major Maastrichtian gateways

Figure DR3. Temperature trends at different ocean depths for the 2× and 4× PI CO_2 simulations

Figure DR4. Evolution of the maximal intensity of the Meridional Overturning Circulation

Figure DR5. Maximal late Southern Hemisphere winter mixed-layer depth

Figure DR6. Modeled surface water salinities in the Maastrichtian for the 2× and 4× PI CO_2 simulations

Figure DR7. Mean annual freshwater fluxes from runoff

Figure DR8. Meridional Overturning Circulation for the 2×, and 4× PI CO_2 Maastrichtian simulations, as well as the difference between the simulations.

Figure DR9. Deep and intermediate net water transports across major gateways in the 4× PI CO_2 Maastrichtian simulation

References

Bottom water temperature records in the Maastrichtian in the Pacific vs. the high-latitude South Atlantic and proto-Indian sectors of the Southern Ocean

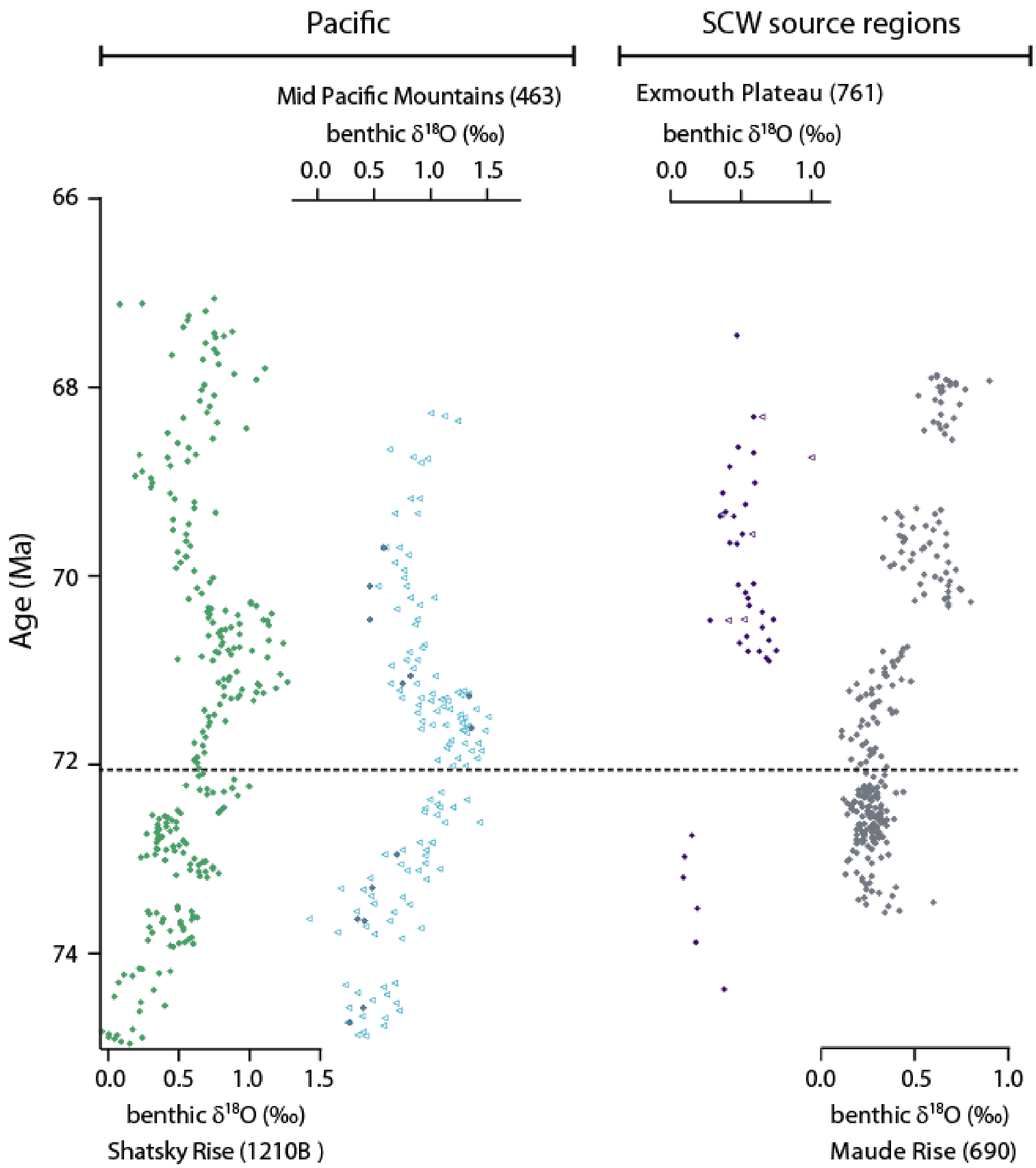

Figure DR1. Compilation of benthic foraminiferal $\delta^{18}O$ from the Pacific and South Atlantic and proto-Indian sectors of the Southern Ocean. Benthic foraminiferal $\delta^{18}O$ data sources: Site 463 (Barrera et al., 1997; Li and Keller, 1999), 690 (Friedrich et al., 2009), 761 (Barrera, 1994; MacLeod and Huber, 1996), and 1210 (Jung et al., 2013). Absolute ages are updated to the 2012 Geologic times scale (Gradstein et al., 2012). Tie points used in age models for Sites 690, 761, and 1210 are as follows (Site 463 described in detail below): Hamilton, 1990; Huber, 1990; Bralower and Siesser, 1992; Galbrun, 1992, Jung et al., 2013 (and references therein).

Site locations and paleogeography

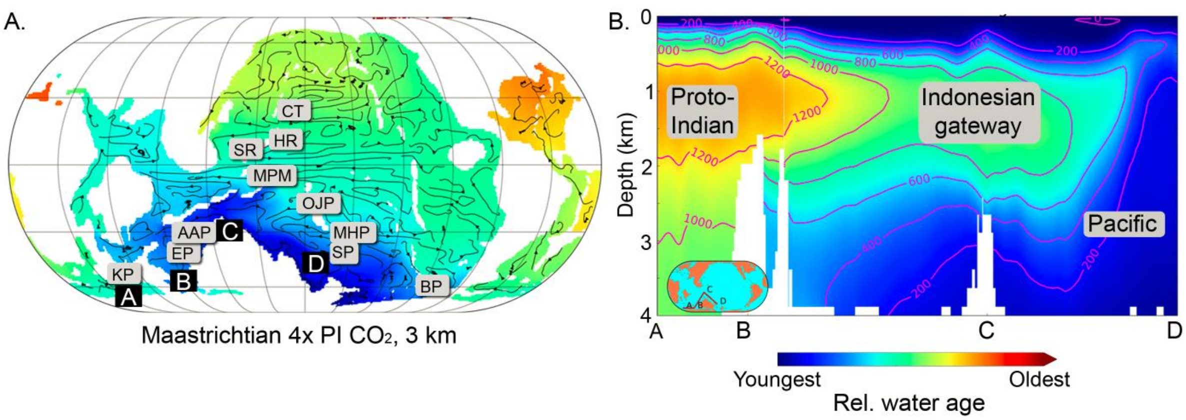

Figure DR2. (A) Map-view paleogeographic reconstruction of the Maastrichtian ocean at 3 km water depth that includes simulated water age with 4× pre-industrial (PI) CO_2 concentrations (after Text Fig. 4). Gray boxes indicate the locations of relevant Pacific and Indian Ocean sites as follows: AAP - Argo Abyssal Plain, BP - Bellingshausen Abyssal Plain, CT - Chinook Trough, EP - Exmouth Plateau, HR - Hess Rise, KP - Kerguelen Plateau, MHP - Manihiki Plateau, MPM - Mid Pacific Mountains, OJP - Ontong Java Plateau, SP - South Pacific, and SR - Shatsky Rise. Black boxes indicate endpoints for segments in the cross section shown in panel (B). (B) Vertical profile of simulated water age (Maastrichtian, 4× PI CO_2) is an east-west trending transect from the proto-Indian Southern Ocean, across the Indonesian Gateway into the southwest Pacific Ocean connecting points A-D in panel (A). The depth transect indicates that the only region in which young waters extend from the sea surface to the sea floor is at point D, with waters being progressively older with distance from that point.

Table DR1. Paleogeographic and bathymetric information

Site	Location	Paleo. Lat.	Paleowater Depth (m)	Refs. for Paleo Lat. and depths
289	Ontong Java Plateau (OJP)	~10° S	~2,500	Mahoney et al., 2001; MacLeod and Bergen, 2004
317	Manihiki Plateau (MHP)	~30° S	2,000-3,000	MacLeod and Bergen, 2004
323	Bellingshausen Abyssal Plain (BP)	67° S	~2,000	Hollister et al., 1976; Thomas et al., 2014
463	Mid Pacific Mountains (MPM)	~5° S	1500–2,000	Boersma, 1981; Moiroud et al., 2016
464	Northern Hess Rise (HR)	~10–14° N	below CCD ~4,000	Thiede and Rea, 1981; Roth, 1981; Moiroud et al., 2016
465	Southern Hess Rise (HR)	~4–12° N	~900-1,500	Barrera and Savin, 1999; Roth, 1981; Thiede and Rea, 1981, Vallier et al., 1981
596	South Pacific (SP)	38° S	5,000	Thomas et al., 2014 (for the Paleocene)
886	Chinook Trough (CT)	Mid-northern lat.	>4,400	Moiroud et al., 2016
1186	Ontong Java Plateau (OJP)	~10° S	~2,800	Mahoney et al., 2001; MacLeod and Bergen, 2004
1208	Shatsky Rise (SR)	15° N	1,500–2,500	Bralower et al., 2002; Murphy and Thomas, 2012
1209	Shatsky Rise (SR)	~10–15° N	~2,300	Bralower et al., 2002; Thomas, 2004; Murphy and Thomas, 2012
1210	Shatsky Rise (SR)	~10° N	~2,300–2,500	Bralower et al., 2002; Frank et al., 2005; Jung et al., 2013
1211	Shatsky Rise (SR)	~10° N	~2,900	Bralower et al., 2002; Thomas, 2004

Sample processing and analytical methods

Sample preparation

Samples were soaked in kerosene, disaggregated using a Calgon-peroxide solution then washed on a 63 µm screen. To concentrate fish remains (bioapatite) in samples containing abundant foraminifera and other calcareous material in the washed residues, selected samples were acidified using 1M $C_2H_4O_2$ (acetic acid), rinsed in DI water and again washed on 63 µm screen.

REEs and Nd extractions

Fossilized fish debris, including teeth, scales, and bone fragments were picked with a targeted minimum of 200 µg of bioapatite per sample; however, due to the scarcity of fish debris in many samples, samples as small as 20 µg were analyzed. Fish debris was dissolved overnight in aqua regia then dried. To correct ε_{Nd} values for the ingrowth of ^{143}Nd by radioactive decay of ^{147}Sm (equations below), rare earth element (REE) concentrations were measured and averaged for 2–5 samples from each site using an Element ICP-MS at the University of Florida. To do this, samples were dissolved in HNO_3 and an aliquot was spiked with a rhodium-rhenium solution prior to analysis. Samples were diluted relative to the raw fish debris weight using 1 N HNO_3.

To isolate REEs for Nd isotopic analysis, samples were dissolved in 1N HNO_3 and run through columns filled with Eichrom TruSpec resin. The aliquots were dried and re-dissolved in 0.25 N HCL and run through columns filled with Eichrom Ln-spec resin to volumetrically separate Nd from the other REEs.

Neodymium isotopic (ε_{Nd}) analyses

For ε_{Nd} analyses, samples were introduced into a Nu Plasma MC-ICP-MS (at the University of Florida) using a DSN-100 nebulizer and concentrations of ^{143}Nd and ^{144}Nd were measured with each sample being which were diluted with 2% HNO_3 until a target ^{143}Nd beam voltage of ~3–5 V was achieved. To monitor external precision of the instrument the synthetically created international standard, JNdi-1 ($^{143}Nd/^{144}Nd$ = 0.512103), was run every 6 samples. External reproducibility for JNdi-1 standards is +/- 0.27 ε_{Nd} units (2σ) and is used as a minima for internal error values included on Fig. 2.

Following the conventions of DePaolo and Wasserburg (1976), neodymium isotopes are reported relative to deviation of $^{143}Nd/^{144}Nd$ from the chondritic uniform reservoir (CHUR) in parts per ten thousand using the ε_{Nd} notation. The following equations were used to calculate $\varepsilon_{Nd(0)}$ (the present ε_{Nd} ratio) and $\varepsilon_{Nd(t)}$ (the ε_{Nd} ratio at time "t" when the Nd was incorporated into the bioapatite at the seafloor, correcting for the subsequent decay of ^{147}Sm to ^{143}Nd following deposition). All values are reported in Table DR2 (below).

(1) $\varepsilon_{Nd(0)} = [(^{143}Nd/^{144}Nd)_{sample(0)}/(^{143}Nd/^{144}Nd)_{CHUR(0)} - 1]x10^4$

Where $(^{143}Nd/^{144}Nd)_{sample(0)}$ = the measured $^{143}Nd/^{144}Nd$ ratio, and $(^{143}Nd/^{144}Nd)_{CHUR(0)}$ = 0.512638.

(2) $\varepsilon_{Nd(t)} = [(^{143}Nd/^{144}Nd)_{sample(t)}/(^{143}Nd/^{144}Nd)_{CHUR(t)} - 1]x10^4$

Where $(^{143}Nd/^{144}Nd)_{sample(t)} = [(^{14\ 3}Nd/^{144}Nd)_{sample(0)} - (^{147}Sm/^{144}Nd)_{sample(0)}(e^{\lambda t}-1)]$, $(^{143}Nd/^{144}Nd)_{CHUR(t)} = [(^{143}Nd/^{144}Nd)_{CHUR(0)}-(^{147}Sm/^{144}Nd)_{CHUR(0)}(e^{\lambda t}-1)]$, $(^{143}Nd/^{144}Nd)_{CHUR(0)}$ = 0.512638, $(^{147}Sm/^{144}Nd)_{CHUR(0)}$ = 0.1967, and $(^{147}Sm/^{144}Nd)_{sample}$ = average of measured $^{147}Sm/^{144}Nd$ per site, λ = 0.0000065, and t = estimated time of sediment deposition.

Table DR2: Neodymium isotopic data

Core-section, interval	Depth (mbsf)	Age (Ma)	$^{143}Nd/^{144}Nd$	$\varepsilon_{Nd(0)}$	$\varepsilon_{Nd(t)}$	2σ^{+}
DSDP Site 289						
123-1, 110-112 cm	1156.10	66.92	0.512319	-6.22	-5.62	0.23
124-2, 11-13 cm	1166.11	67.91	0.512268	-7.22	-6.61	0.20
127-1, 131-133 cm	1194.31	71.29	0.512358	-5.46	-4.82	0.24
128-1, 123-125 cm	1203.73	73.50	0.512386	-4.92	-4.25	0.36
129-1, 115-117 cm	1213.15	75.72	0.512367	-5.28	-4.60	0.23
Average $^{147}Sm/^{144}Nd$ for Site 289		*0.125712*				
DSDP Hole 317A						
3-1, 44-46 cm	563.94	69.01	0.512350	-5.61	-4.99	0.24

	3-1, 130-132 cm	564.80	69.12	0.512325	-6.11	-5.48	0.34
	3-2, 128-130 cm	566.28	69.38	0.512352	-5.58	-4.96	0.18
	3-3, 125-127 cm	567.75	69.64	0.512360	-5.42	-4.80	0.26
	3-4, 60-62 cm	568.60	69.79	0.512399	-4.66	-4.03	*0.43*
	Average $^{147}Sm/^{144}Nd$ for Site 317		*0.125756*				
DSDP Site 463							
	7-3 75-90 cm	47.25	**68.28**	0.512387	-4.90	**-4.20**	0.26
dup.	7-3 75-90 cm	47.25	**68.28**	0.512371	-5.20	**-4.51**	0.22
dup.	7-3, 75-90 cm	47.25	**68.28**	0.512392	-4.79	**-4.10**	*0.43*
	8-3 15-30 cm	56.15	**68.77**	0.512357	-5.48	**-4.78**	0.32
	11-2, 40-55 cm	83.40	**70.25**	0.512352	-5.58	**-4.87**	0.26
dup.	11-2, 40-55 cm	83.40	**70.25**	0.512343	-5.76	**-5.04**	0.21
	12-2, 35-50 cm	92.85	**70.77**	0.512318	-6.24	**-5.52**	0.25
dup.	12-2, 35-50 cm	92.85	**70.77**	0.512319	-6.22	**-5.50**	0.20
dup.	12-2, 35-50 cm	92.85	**70.77**	0.512308	-6.44	**-5.72**	0.23
	12-5, 35-50 cm	97.35	**71.01**	0.512323	-6.15	**-5.43**	0.21
	13-2, 35-50cm	102.35	**71.29**	0.512333	-5.96	**-5.24**	0.17
	13-4, 35-50 cm	105.35	**71.45**	0.512345	-5.72	**-4.99**	0.20
	14-2, 35-50 cm	111.85	**71.80**	0.512334	-5.93	**-5.20**	0.30
	14-4, 115-130 cm	115.65	**72.01**	0.512335	-5.91	**-5.18**	0.20
	15-1, 35-50 cm	119.85	**72.24**	0.512332	-5.96	**-5.23**	0.22
	15-3, 35-50 cm	122.85	**72.40**	0.512328	-6.05	**-5.31**	0.23
	15-5, 35-50 cm	125.85	**72.57**	0.512330	-6.00	**-5.27**	0.26
	16-1, 100-115 cm	130.00	**72.79**	0.512341	-5.79	**-5.05**	0.21
	16-3, 75-90 cm	132.75	**72.94**	0.512352	-5.58	**-4.84**	0.21
	16-6, 35-50 cm	136.32	**73.14**	0.512341	-5.79	**-5.05**	0.20
	19-2, 35-50 cm	159.35	**74.39**	0.512351	-5.59	**-4.84**	0.20
	19-5, 35 -50 cm	163.85	**74.64**	0.512355	-5.53	**-4.77**	0.33
dup.	19-5, 35-50 cm	163.85	**74.64**	0.512353	-5.56	**-4.80**	0.25
	21-2, 35-50 cm	178.35	**75.43**	0.512333	-5.95	**-5.18**	0.17
dup.	21-2, 35-50 cm	178.35	**75.43**	0.512329	-6.03	**-5.26**	0.30
	22-2, 35-50 cm	187.85	**75.94**	0.512353	-5.55	**-4.78**	0.21
dup.	22-2, 35-50 cm	187.85	**75.94**	0.512365	-5.33	**-4.55**	0.17
	23-1, 35-50 cm	195.85	**76.38**	0.512369	-5.25	**-4.47**	0.18
dup.	25-1, 35-50 cm	205.35	**76.90**	0.512344	-5.74	**-4.96**	0.23
	Average $^{147}Sm/^{144}Nd$ for Site 463		*0.116552*				
ODP Hole 1186A							
	13-CC	803.85	63.00*	0.512367	-5.29	-4.68	0.25
	16-CC	833.09	69.73	0.512340	-5.81	-5.14	0.24
	17-CC	844.17	70.07	0.512314	-6.32	-5.64	0.33
	19-CC	861.35	70.63	0.512324	-6.13	-5.44	0.37

20-CC	870.78	71.65	0.512364	-5.34	-4.65	0.20
22-CC	890.19	73.77	0.512372	-5.19	-4.47	0.21
Average $^{147}Sm/^{144}Nd$ for Site 1186		*0.120200*				

Footnotes:

dup. = duplicate, values were averaged on plots

Calculations for $\varepsilon_{Nd(0)}$ and $\varepsilon_{Nd(t)}$ can be found in "Sample processing and analytical methods" section of this supplement

⁺ Error bars plotted on Fig. 2 for Sites 463 and 1186 have a minimum of 0.27 which is the external precision of Jndi-1 standards on the instrument. Nd isotopic values with a 2σ error > 0.40 were not included in plots

* Unsure of age

Age models for DSDP Sites 289, 317, 463, and ODP Site 1186

The age models presented here are based on the first and last occurrences of relevant foraminiferal and calcareous nannoplankton species which are listed in Table DR3 for each site. Absolute ages were updated to be consistent with the 2012 Geologic Time Scale (Huber et al., 2008; Gardin et al., 2012; Gradstein et al., 2012; Watkins pers. comm.).

For DSDP Site 463, both foraminiferal and nannoplankton communities have been well-studied, and thus, both groups were included (Thiede et al., 1981; Li and Keller, 1999). In addition, the Campanian-Maastrichtian boundary was also used at this sites as it can be identified by a minima among benthic foraminiferal $\delta^{13}C$ values which also served as an anchor to correlate this site with Site 1210 on Shatsky Rise (Fig. 2). A best fit line through the events was used to calculate absolute ages.

Age models for sites on Ontong Java Plateau (DSDP Site 289, ODP Site 1186) and Manihiki Plateau (DSDP Site 317) were generated using calcareous nannoplankton events that were updated to be consistent with the 2012 geologic time scale (Gardin et al., 2012; Gradstein et al., 2012; Watkins, pers. comm.). Due to the limited number of events identified at these sites point-to-point extrapolation (i.e., the slopes between each of the events, rather than a best fit line) was used to calculate age (Table DR3).

Table DR3. Events used for each age model

Event description	Event depth (mbsf)	Age (Ma)	Event citation	Age citation
DSDP Site 289				
K/Pg boundary	1146.8	66.0	Andrews et al., 1975	Gradstein et al., 2012
FA *Micula murus*[N]	1166.0	67.9	Andrews et al., 1975	Huber et al., 2008
FA *Lithoquadratus quadratus*[N]	1185.0	69.1	Andrews et al., 1975	Gardin et al., 2012
FA *Uniplanarius trifidus*[N]	1213.5	76.8	Andrews et al., 1975	Huber et al., 2008; Gradstien et al., 2012
DSDP Hole 317A				
FA *Micula murus*	554.7	67.9	Schlanger et al., 1976	Huber et al., 2008
FA *Lithoquadratus quadratus*[N]	564.7	69.1	Schlanger et al., 1976	Gardin et al., 2012
FA *Arkhangelskiella cymbiformis*[N]	573.2	70.6	Schlanger et al., 1976	Gardin et al., 2012
FA *Uniplanarius trifidus*[N]	582.5	76.8	Schlanger et al., 1976	Huber et al., 2008; Gradstein et al., 2012
ODP Hole 1186A				
FA *Lithoquadratus quadratus*[N]	812.9	69.1	MacLeod and Bergen, 2004	Gardin et al., 2012
FA *Arkhangelskiella cymbiformis*[N]	861.1	70.6	MacLeod and Bergen, 2004	Gardin et al., 2012
FA *Uniplanarius trifidus*[N]	908.8	76.8	MacLeod and Bergen, 2004	Huber et al., 2008; Gradstein et al., 2012
DSDP Site 463				
FA *Contusatruncana contusa* (*Rosita contusa*)[F]	88.0	71.0	Li and Keller, 1999	Gradstein et al., 2012
Campanian-Maastrichtian boundary (indicated by benthic foraminiferal $\delta^{13}C$ minimum)	132	72.1	Depth modified from Ando et al., 2009	Gradstein et al., 2012
FA *Globotruncana aegyptiaca*[F]	164.5	74.0	Li and Keller, 1999	Gradstein et al., 2012
LA *Radotruncana calcarata*[F]	176.7	75.7	Li and Keller, 1999	Gradstein et al., 2012
FA *Radotruncana calcarata*[F]	192.5	76.1	Li and Keller, 1999	Gradstein et al., 2012

FA *Uniplanarius trifidus*[N]	195.8	76.8	Thiede et al., 1981	Huber et al., 2008; Gradstein et al., 2012

Footnotes

[F] indicates a planktonic foraminiferal datum event

Details of ocean climate model simulations

Description of models

The simulations presented in this manuscript have been run using the Community Climate System Model version 4 (CCSM4) on resources provided by the National Center for Atmospheric Research (NCAR). CCSM4 is comprised of the Community Atmospheric Model version 4 (CAM4), the Community Land Model version 4 (CLM4) with either dynamic or prescribed vegetation, the Parallel Ocean Program model version 2 (POP2) and the Community Sea Ice model version 4 (CICE4). POP2 and CICE4 were run on a rotated poles grid at roughly 1° resolution with 60 uneven vertical levels in the ocean. CAM4 and CLM4 were run on a finite-volume grid at 1.9°x2.5° resolution with 28 uneven vertical levels in the atmosphere.

Models setup

Two sets of simulations were run using a Maastrichtian paleogeographic reconstruction of Getech Plc. In the first set, CCSM4 was run for 1500 years with dynamic vegetation and atmospheric CO_2 levels of either 4× (1120 ppm) or 2× (560 ppm) preindustrial atmospheric levels. Other greenhouse gas concentrations were set to preindustrial values. The orbital configuration of the Earth is present-day and the incoming total solar irradiance was adjusted to the appropriate Maastrichtian value following Gough (1981). For additional details on this set of simulations, see Tabor et al. (2016) in which this set of results was analyzed and compared to proxy data and simulations from the UK HadCM3L model.

The second set of simulations are extensions of the two 1500 year simulations using prescribed vegetation based on Sewall et al. (2000). Other boundary conditions do not change. The 4× CO_2 simulation was integrated for a total of 1800 additional years and the 2× CO_2 simulation for a total of 1350 years. The history of the model spin up toward equilibrium for both simulations is discussed in the section “Simulations equilibrium”. Results presented in the manuscript and Supplementary Information use the average of the last 100 years each simulation.

Paleogeography

We used the Maastrichtian paleogeography from Tabor et al. (2016) (Fig. 1). This reconstruction was created by Getech Plc using methods described in Markwick and Valdes (2004) and Lunt et al. (2016).

The Maastrichtian paleogeography features shallow Caribbean and Drake seaways. Variations in the depth of these gateways has been shown to have a large impact on Cretaceous ocean circulation (Donnadieu et al., 2016), but shallow gateways in these regions are in agreement with most studies. The timing of the opening of Drake Passage to intermediate and deep flow is still debated but probably took place between the Eocene and the Miocene (e.g., Eagles et al., 2006; Lagabrielle et al., 2009; Eagles and Jokat, 2014). Prior to 50 Ma, the geometry and depth of Drake Passage are not well constrained either (e.g. Vérard et al., 2012; Lawver et al., 1992; Markwick and Valdes, 2004), but, if open to exchange between the Pacific and southern South Atlantic, its depth was shallow (Lawver et al., 1992).

The geological and oceanographic history of the Caribbean Seaway is also complex and not completely understood (see review in Iturralde-Vinent, 2006). There is evidence that island arc volcanism was active during the Late Cretaceous in the Caribbean region (Iturralde-Vinent and McPhee, 1999; Pindell et al., 2006) with two main volcanic archipelagos generally cited. One arc was located in the oceanic gap between North and South America (the Antillean volcanic arc system, terminology of Iturralde-Vinent, 2006), which is responsible for the shallow passage in our reconstruction, and the other arc westward in the Pacific Ocean (Iturralde-Vinent, 2006, see e.g. their fig. 5B). The Antillean arc system is unlikely to have formed a permanent land bridge between North and South America. Rather, it was probably a system of islands and shallows (Iturralde-Vinent, 2006 and references therein) that restricted water flow between the Pacific and Caribbean Basin and potentially provided temporary land connection and/or opportunities for island-hopping that allowed for terrestrial faunal exchange (e.g., Gayet, 2001; Ortiz-Jauregizar and Pascual, 2011).

We acknowledge however that some previous work has used alternative Caribbean Seaway configurations in Late Cretaceous modeling studies, most notably the work of Donnadieu et al. (2016), whose paleogeographic reconstruction is based on that of Sewall et al.

(2007). The paleogeographic reconstruction in Sewall et al. (2007) features an open Caribbean Seaway in the Albian, Aptian, and Cenomanian, that widens and deepens with time. However, an explicit goal in Sewall et al. (2007) is to provide Cretaceous boundary conditions “that can be easily incorporated as the lower boundary condition of a GCM”. In doing so, the complexity of the paleogeography was intentionally reduced to allow for easier implementation into numerical models. Specifically, for the Caribbean region, islands which would have restricted flow between North and South America were removed, even though the underlying paleogeographic reconstructions they used indicate Caribbean islands from the Cenomanian onwards (Sewall et al., 2007).

Due to abundant evidence that supports islands and shallow water-depths along the Antillean volcanic arc system in the Late Cretaceous, the paleogeography used here limits flow across the Caribbean Seaway to surface waters. Further, we note that progressive restriction of flow through the Caribbean Seaway has been invoked to explain changes in ε_{Nd} values in North Atlantic sites (MacLeod et al., 2008; 2011), but, to avoid circularity, interpretations of ε_{Nd} data were not used to guide decisions about tectonic configurations.

Simulations equilibrium

The timeseries of temperature and maximal intensity of the Meridional Overturning Circulation for the second set of simulations are shown on Figs. DR3 and DR4. Both simulations have reached near-equilibrium. A small residual trend exists in the intermediate ocean of the 4× PI CO_2 simulation (500 and 1000 m temperatures, Fig. DR3), which is probably related to the intensification of the MOC in this simulation (Fig. DR4). This trend, however, does not affect conclusions of this study because the shape of the ocean circulation patterns do not change between the simulations, or during the interval of lower MOC intensity, and the MOC intensity has also stabilized (Fig. DR4).

On the other hand, the intensification of the MOC in the 4× PI CO_2 simulation (relative to the integration time) between model years 2100 and 2500 would introduce a potential artifact in calculation of the absolute water ages for this simulation. The ideal age tracer of water masses (IAGE) works as an “integrator” of the oceanic circulation, which means that any significant change in the oceanic circulation will impact IAGE values at least on a timescale of the ocean mixing time (1500–2000+ years). In other words, to obtain meaningful IAGE values the model needs to be integrated for another ~ 2000 years once a stable oceanic circulation is reached. Unfortunately, we did not have the resources to extend the models further. So, while maximum overturning rates in the 4× PI CO_2 simulation are always lower than maximum overturning rates in the 2× PI CO_2 simulation and both models seem to have stabilized by the end of their respective simulation, we only use the water ages as a qualitative indicator (as on Fig. 4) that illustrates similarities in patterns and relative differences in rates of ocean circulation with 4× vs. 2× PI CO_2 conditions.

Maastrichtian ocean circulation

In this section, we describe the ocean circulation patterns in the two simulations and show diagnostics that support the intensification of the circulation in the lower CO_2 simulation as a way to explain the shift to more non-radiogenic ε_{Nd} values during the EMCP.

In both simulations, the maximal late winter mixed-layer depths (Fig. DR5) and the water ages in the deep (Fig. 4) reveal that deep-water formation takes place in the southwest Pacific as the result of the winter cooling of salty upper ocean water masses (Fig. DR6). Salinity is higher in the South Pacific than in other high latitudes regions because of a deficit in freshwater supply from runoff (Fig. DR7) and of the salt-advection feedback that characterizes deep-water formation regions: sinking waters drive the advection of warm and salty subtropical waters to the high latitudes. This leads to anomalously dense upper ocean waters when temperatures decrease during the winter season and thus fuels the deep-water formation.

This unipolar deep-water formation drives a Meridional Overturning Circulation (MOC) that significantly differs from the modern (Fig. DR8). In both simulations, the MOC is constituted of a large counterclockwise overturning cell, with a maximum around 35°S and 2000 m depth and whose lower limb reaches the northern mid to high latitudes. The main pathways of water masses can be assessed by calculating the water transports across major oceanic gateways (Donnadieu et al. 2016). Table DR4 presents surface, intermediate and deep water transports across major gateways for the two simulations and show that the oceanic circulation pattern is the same regardless of the prescribed CO_2 concentrations. In details, after they sink in the southwest Pacific, deep water masses are advected across the Indonesian gateway into the South Indian Ocean and the Tethyan Ocean (Fig. DR9, shown for the 4× PI CO_2 simulation). Because the Tethyan connection to the Atlantic Ocean is very shallow in our reconstruction, the deep water masses are advected towards the North Atlantic via the South Indian and Atlantic oceans which is consistent, in terms of flow direction, with previous interpretations of ε_{Nd} records by Robinson and Vance (2012). As the Caribbean seaway is closed to deep and intermediate circulation, the deep waters reaching the North Atlantic are upwelled to shallower (intermediate) depths and journey back southward to the Southern Atlantic and Indian oceans and ultimately to the Pacific (Fig. DR9).

Interestingly, even though circulation patterns are identical, the 2× PI CO_2 MOC intensity is slightly enhanced by ~1–2 Sv relative to the 4× PI CO_2 MOC (Figs. DR4, DR8), which supports more vigorous oceanic circulation under lower CO_2 levels. This is confirmed by the water transports in the 2× PI CO_2 experiment (Table DR4), which are consistently slightly larger than in the 4× PI CO_2 case.

Comparison to previous modeling efforts

Comparisons between Cenomanian and Maastrichtian model results that use the same CCSM4 and UK HadCM3L models as us, as well as between model and proxy results were presented in Tabor et al., 2016. Both comparisons yielded reasonable agreement given uncertainties in paleogeographic reconstructions, proxy estimates and model parameterizations and resolutions. They will therefore not be performed here again.

To our knowledge, the study of Donnadieu et al. (2016; hereafter D16) is the only modeling study that explores, in detail, the deep ocean circulation patterns of the Late Cretaceous (Turonian– Maastrichtian). As stated in the text, an important similarity between the D16 modeling study and ours is that both show a weak sensitivity of large scale patterns ocean circulation to moderate changes in CO_2 concentrations (and, so, temperature) using Late Cretaceous paleogeography. Differences between the studies relate to specific circulation patterns predicted, that likely result from the combined effects of different boundary conditions (in particular, the Maastrichtian paleogeography) as well as differences in complexity and resolution in the models used (CCSM4 in this study and FOAM in D16).

The D16 Maastrichtian control experiment produces a completely different pattern of oceanic circulation than our simulations. The locations of deep-water formation and the geometry of a number of gateways are different. In particular, their Maastrichtian control experiment has a deep Caribbean Seaway whereas in our reconstruction the seaway is closed to intermediate and deep water flow. Their simulation produces deep-water formation in the North Pacific and in the Atlantic and Indian sectors of the Southern Ocean (D16 fig. 1). Part of the deep waters formed in the Southern Ocean are advected northward into the Atlantic (fig. 2 of D16) then flow across the Caribbean Seaway in the Pacific, where they mix in with deep water formed in the North Pacific. The other part of the deep waters formed in the Southern Ocean are advected northward across the East Indian seaway, but it remains unclear from the published results of D16 whether these deep waters next enter the Pacific or flow towards the Tethyan Ocean. An interesting feature in the D16 results is that when the Caribbean seaway is reduced to 560 m (the configuration they test which is the closer to our Caribbean seaway), the direction of deep circulation in the Atlantic reverses from a northward dominated flow to a southward dominated flow (except in the deepest layer and without any change in deep water formation region, see D16 fig. 8 and 9).

Contrasting patterns of ocean circulation between the two studies (i.e., ours vs. D16) can be explained by the different locations of deep water formation. In D16 simulations, deep water formation is formed in the Southern Indian and Atlantic oceans, and water advection in the deep will therefore be along directions away from these areas. In contrast, in our simulation, deep waters are exported away from the southwestern Pacific towards the Indian Ocean (and the southeastern Pacific). This explains why deep water advection across the East Indian gateway is northward in D16 and southward in our experiments.

Maastrichtian Gateways	Water transport (Sv)			
	Surface (0 - 300 m)	Intermediate (300 - 1500 m)	Deep (> 1500 m)	Total
Caribbean (positive eastward)	-5.61 (2.64 - 8.25) -5.95 (2.82 - 8.77)	0 0	0 0	-5.61 (2.64 - 8.25) -5.95 (2.82 - 8.77)
Central Atlantic (positive northward)	1.08 (4.38 - 3.30) 1.37 (4.62 - 3.25)	-2.29 (0 - 2.29) -2.50 (0 - 2.50)	1.82 (2.31 - 0.49) 1.93 (2.41 - 0.48)	0.60 (6.69 - 6.08) 0.80 (7.03 - 6.23)
Drake (positive Pacific to Atlantic)	0.79 (1.28 - 0.48) 0.93 (1.26 - 0.33)	0.63 (0.63 - 0) 0.60 (0.60 - 0)	0 0	1.42 (1.91 - 0.48) 1.53 (1.86 - 0.33)
East Indian (positive northward)	4.71 (4.71 - 0) 4.98 (4.98 - 0)	5.31 (5.31 - 0) 5.70 (5.70 - 0)	-3.74 (0.19 - 3.93) -3.69 (0.21 - 3.90)	6.28 (10.21 - 3.93) 7.0 (10.89 - 3.90)
Indo-Asian (positive Tethys to Indo-Pac.)	-10.93 (0.29 - 11.23) -10.91 (0.23 - 11.14)	3.32 (3.32 - 0) 2.37 (2.44 - 0.07)	-2.62 (0 - 2.62) -2.71 (0.23 - 2.95)	-10.23 (3.61 - 13.85) -11.25 (2.90 - 14.16)
Indonesian (positive eastward)	7.48 (8.80 - 1.33) 7.24 (8.61 - 1.37)	8.68 (8.68 - 0) 9.81 (9.81 - 0)	-7.36 (0.66 - 8.02) -7.44 (0.86 - 8.30)	8.80 (18.14 - 9.35) 9.61 (19.28 - 9.67)
Mediterranean (positive eastward)	-6.87 (0 - 6.87) -7.05 (0 - 7.05)	0.44 (0.64 - 0.20) 0.40 (0.61 - 0.22)	0.16 (0.16 - 0) 0.15 (0.15 - 0)	-6.27 (0.80 - 7.07) -6.50 (0.76 - 7.27)
South African (positive eastward)	1.67 (1.68 - 0.01) 1.78 (1.78 - 0)	3.93 (3.93 - 0) 3.94 (3.94 - 0)	-4.09 (0.01 - 4.11) -4.25 (0.01 - 4.27)	1.50 (5.63 - 4.12) 1.47 (5.73 - 4.27)
South Atlantic (positive northward)	0.65 (1.53 - 0.88) 0.92 (1.65 - 0.74)	-3.15 (0 - 3.15) -3.38 (0 - 3.38)	3.11 (3.19 - 0.08) 3.26 (3.34 - 0.08)	0.60 (4.72 - 4.11) 0.80 (4.99 - 4.20)
Tethys (positive Tethys to Indo-Pac.)	-8.60 (2.42 - 11.02) -8.37 (2.84 - 11.20)	3.77 (3.85 - 0.08) 3.33 (3.37 - 0.04)	0 (0.38 - 0.38) 0.03 (0.62 - 0.59)	-4.83 (6.65 - 11.48) -5.0 (6.83 - 12.03)
West Indian (positive northward) – Western side	-6.18 (0 - 6.18) -6.44 (0 - 6.44)	-0.14 (0.56 - 0.69) -0.53 (0.43 - 0.96)	-0.09 (0.03 - 0.11) -0.11 (0.03 - 0.13)	-6.40 (0.59 - 6.98) -7.08 (0.46 - 7.53)
West Indian (positive northward) – Eastern side	2.57 (3.19 - 0.62) 2.71 (3.34 - 0.63)	0.29 (1.12 - 0.83) 0.30 (1.22 - 0.92)	-1.25 (0.16 - 1.40) -1.45 (0.14 - 1.59)	1.62 (4.47 - 2.85) 1.56 (4.70 - 3.14)

Table DR4. Water fluxes across major Maastrichtian gateways for the 4× (black) and 2× (red) PI CO_2 Maastrichtian experiments.

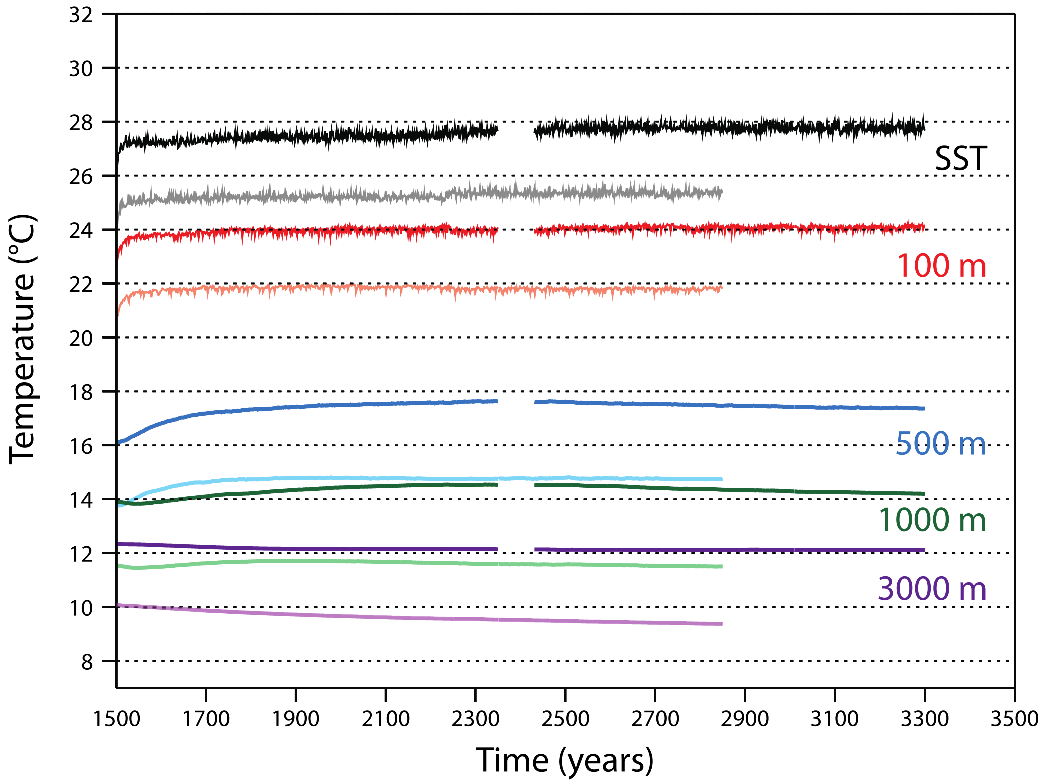

Figure DR3. Temperature trends at different ocean depths for the 4× (darker colors) and 2× PI CO_2 (lighter colors) simulations.

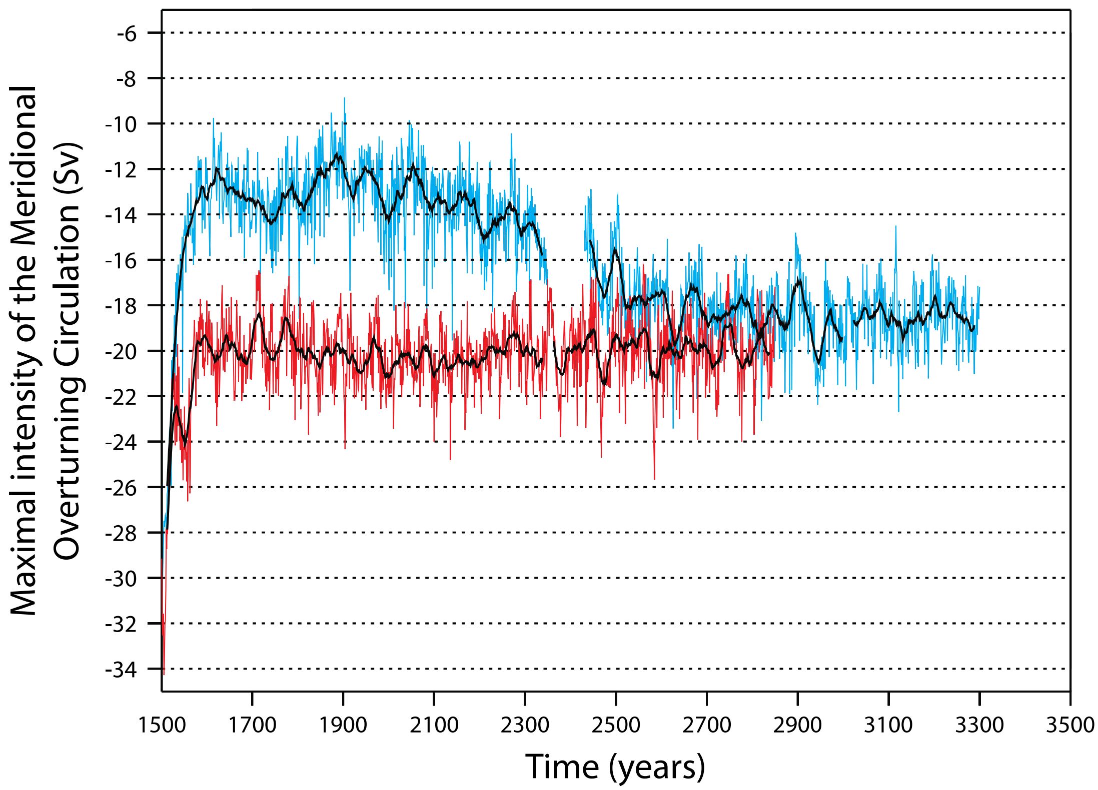

Figure DR4. Evolution of the maximum intensity of the Meridional Overturning Circulation (see Fig. DR8) for the 4× (light blue) and 2× (red) PI CO_2 simulations. Black lines are the 25 years running average. Negative values indicate that the MOC consists primarily of a counterclockwise cell in the Southern Hemisphere (see Fig. DR8).

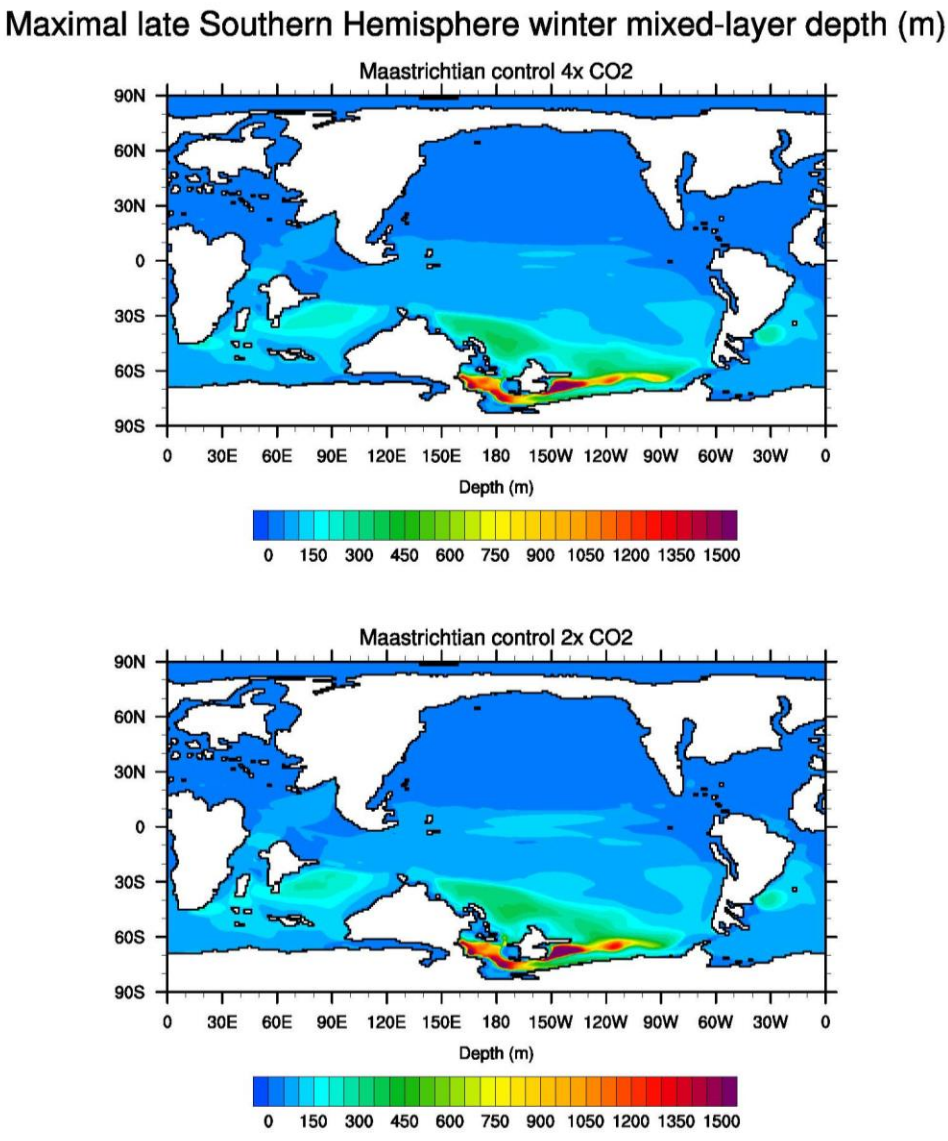

Figure DR5. Maximal late Southern Hemisphere winter (September) mixed-layer depth in the two experiments.

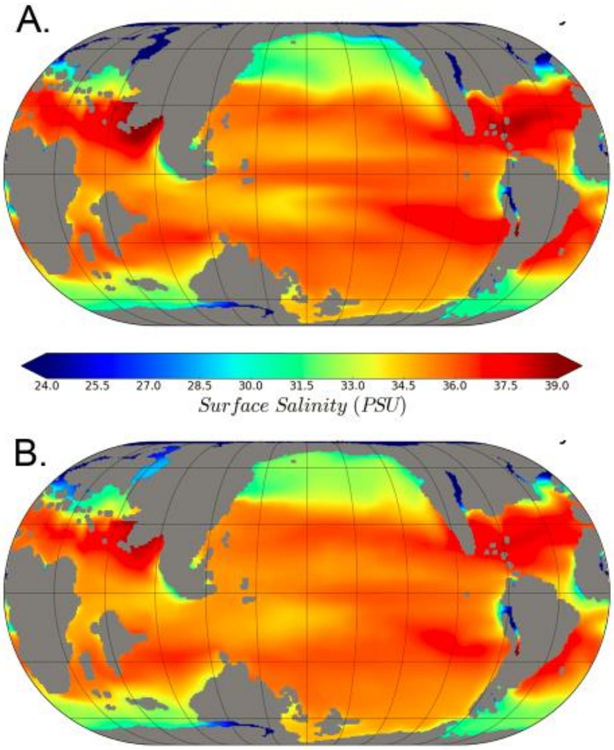

Figure DR6. Modeled surface water salinities in the Maastrichtian (A) with 4× PI CO_2 concentrations and (B) 2× PI CO_2 concentrations. In terms of high latitude regions (> 60° N or S), both simulations show the highest surface salinities in the southern Pacific Ocean.

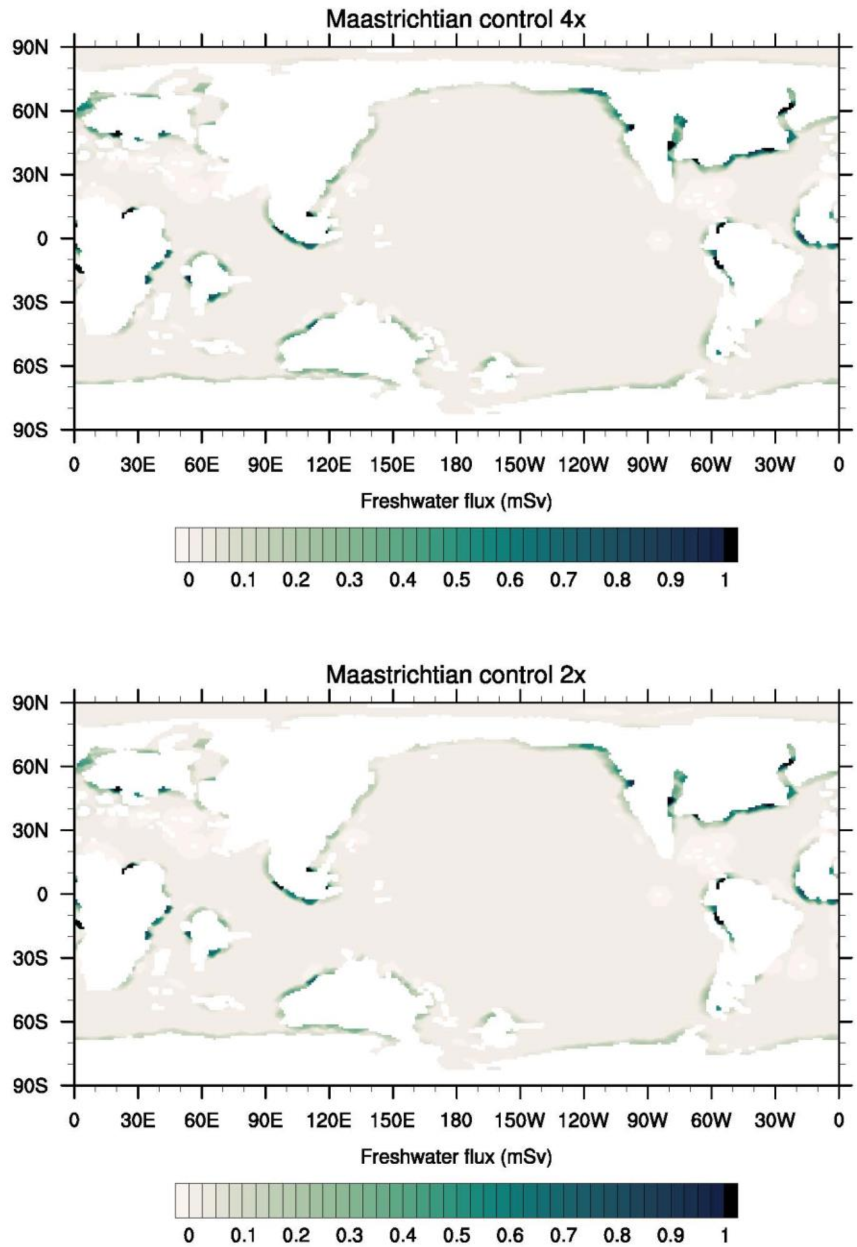

Figure DR7. Mean annual freshwater fluxes from runoff (mSv) for the two Maastrichtian simulations.

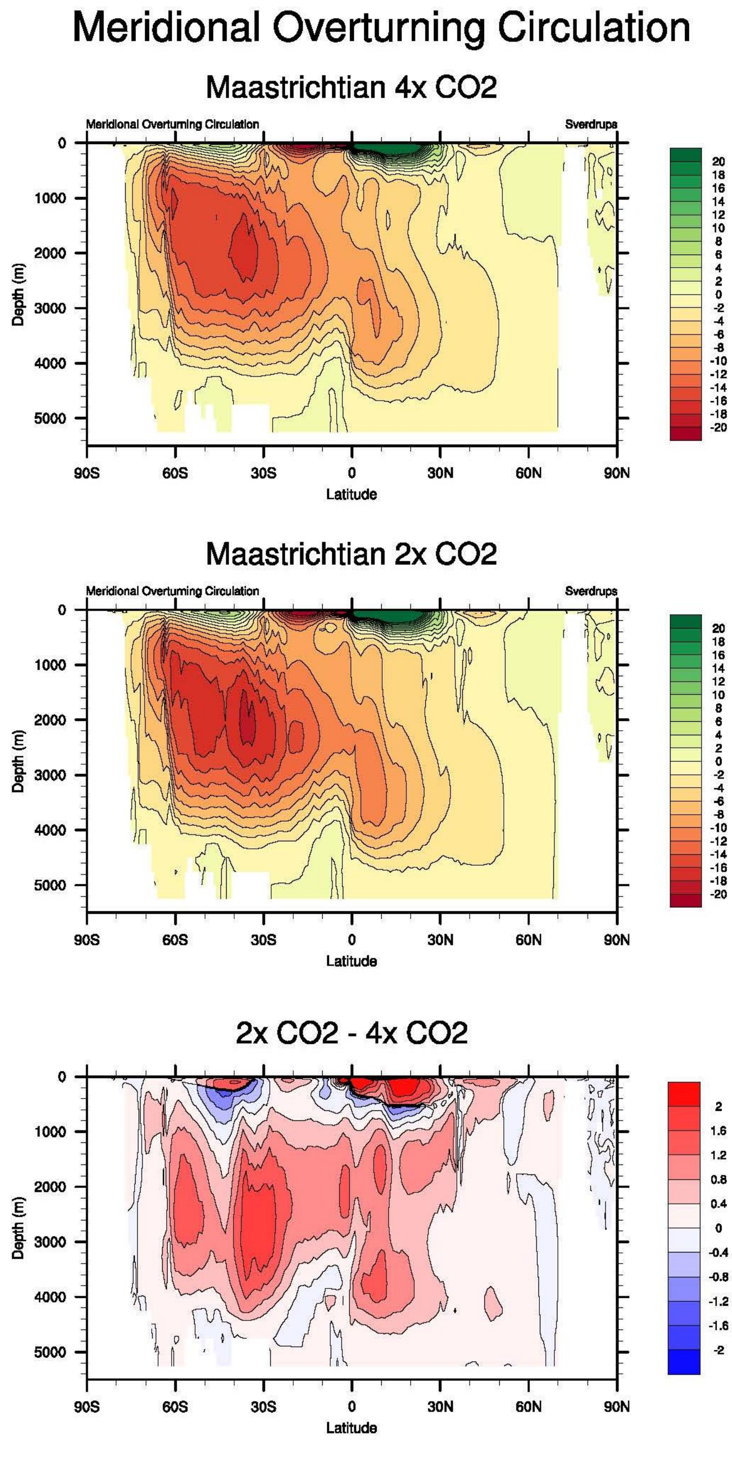

Figure DR8. Meridional Overturning Circulation (Sv) for the 4× (top) and 2× (middle) PI CO_2 Maastrichtian simulations, as well as the absolute difference between the simulations (2× minus 4×, bottom).

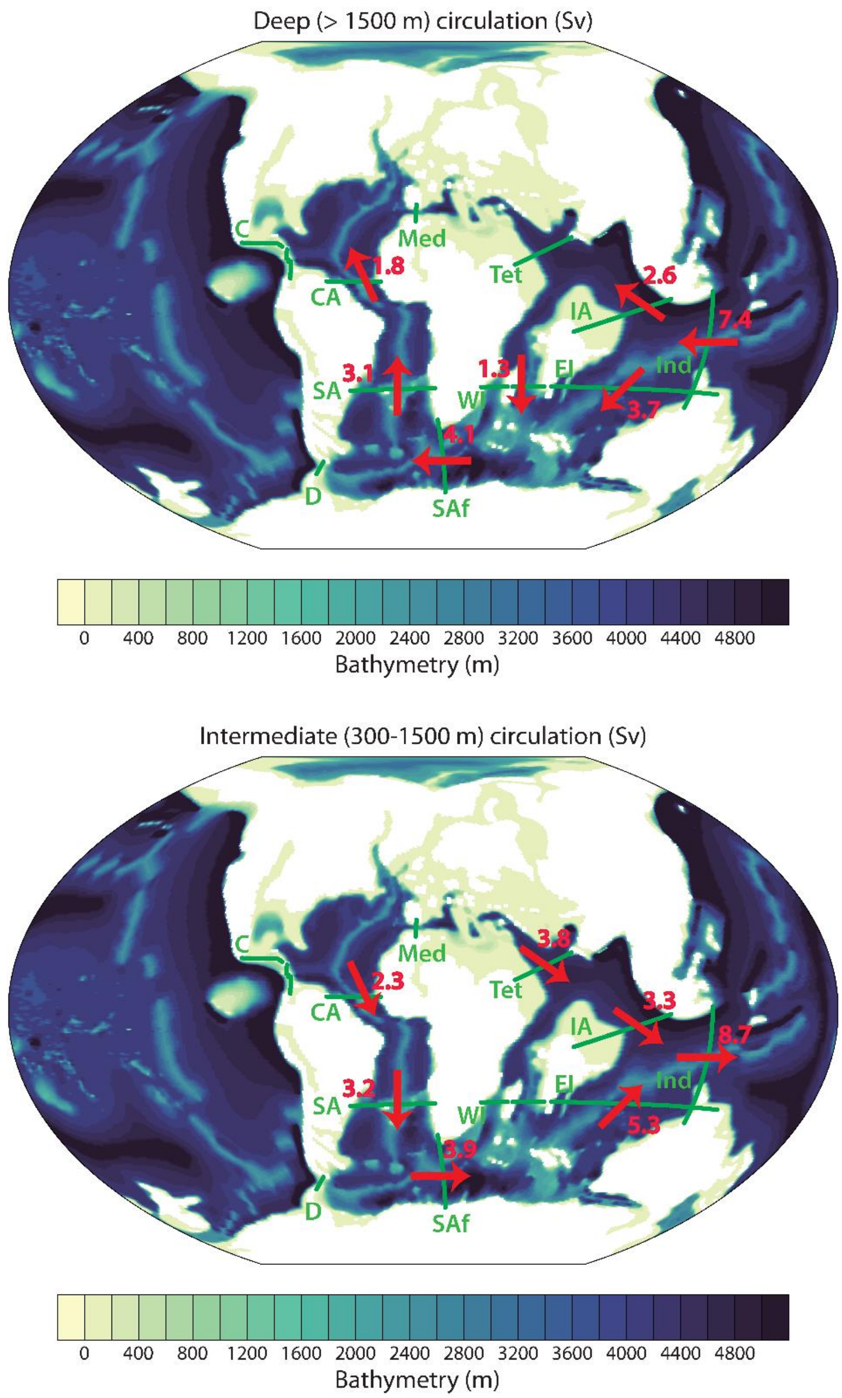

Figure DR9. Deep and intermediate net water transports across major gateways in the 4× PI CO_2 Maastrichtian simulation. The numbers indicate the sum of the positive and negative water transports across the gateway; it does not mean that the water flow is fully unidirectional. C: Caribbean, CA: Central Atlantic, D: Drake, EI: East Indian, IA: Indo-Asian, Ind: Indonesian, Med: Mediterranean, SA: South Atlantic, SAf: South African, Tet: Tethys, WI: West Indian.

References

Andrews, J.E., Peckham, G., 1975, Site 289: Initial Reports of the Deep Sea Drilling Project: Washington (U.S. Govt. Printing Office), v. 30, no. 7, p. 231–398.

Barrera, E., 1994, Global environmental changes preceding the Cretaceous-Tertiary boundary: Early-late Maastrichtian transition: Geology, v. 22, p. 877–880.

Barrera, E., Savin, S.M., Thomas, E., and Jones, C.E., 1997, Evidence for thermohaline-circulation reversals controlled by sea-level change in the latest Cretaceous: Geology, v. 25, no. 8, p. 715–718.

Barrera, E., and Savin, S.M., 1999, Evolution of late Campanian–Maastrichtian marine climates and oceans *in* Barrera, E., and Johnson, C.C., eds., Evolution of the Cretaceous Ocean-Climate System: Boulder, Colorado, GSA Special Paper 332, p. 245–282.

Boersma, A., 1981, Cretaceous and early Tertiary foraminifers from deep sea Drilling Project Leg 62 sites in the Central Pacific: Initial Reports of the Deep Sea Drilling Project, Washington (U.S. Government Printing Office), v. 62, no. 10, p. 377–396, doi:10.2973/dsdp.proc.62.110.1981.

Bralower, T.J., and Siesser, W. G., 1992, Cretaceous calcareous nannofossil biostratigraphy of Site 761, 762, and 763, Exmouth and Wombat Plateaus, northwest Australia, Leg 122, *in* von Rad, U., Haq, B. U., and 26 others: Proceedings of the Ocean Drilling Program, Scientific results, Leg 122: College Station Texas, Ocean Drilling Program, v. 122, p. 529–556, doi:10.2973/odp.proc.sr.122.169.1992.

Bralower, T.J., Premoli Silva, I., Malone, M.J., et al., 2002, Leg 198 summary: Proceedings of the Ocean Drilling Program, Initial Reports, v. 198, no. 1, p. 1–148, doi:10.2973/odp.proc.ir.198.101.2002.

DePaolo, D. J., and Wasserburg, G. J., 1976, Nd isotopic variations and petrogenetic models: Geophysical Research Letters, v. 3, no. 5, p. 249–252.

Donnadieu, Y., Pucéat, E., Moiroud, M., Guillocheau, F., and Deconinck, J. F., 2016, A better-ventilated ocean triggered by Late Cretaceous changes in continental configuration: Nature Communications, v. 7, p. 10316.

Eagles, G., Livermore, R., and Morris, P., 2006, Small basins in the Scotia Sea: the Eocene Drake passage gateway: Earth and Planetary Science Letters, v. 242, no. 3–4, p. 343–353.

Eagles, G., and Jokat, W., 2014, Tectonic reconstructions for paleobathymetry in Drake Passage: Tectonophysics, v. 611, p. 28–50.

Frank, T.D., Thomas, D. J., Leckie, R. M., Arthur, M.A., Bown, P.R., Jones, K., and Lees, J.A., 2005, The Maastrichtian record from Shatsky Rise (northwest Pacific): A tropical perspective on global ecological and oceanographic changes: Paleoceanography, v. 20, p. 1–14.

Friedrich, O., Herrle, J. O., Wilson, P.A., Cooper, M.J., Erbacher, J., and Hemleben, C., 2009, Early Maastrichtian carbon cycle perturbation and cooling event: Implications from the South Atlantic Ocean: Paleoceanography, v. 24, p. PA2211, doi: 10.1029/2008PA001654.

Galbrun, B., 1992, Magnetostratigraphy of Upper Cretaceous and lower Tertiary sediments, Sites 761 and 762, Exmouth Plateau, northwest Australia, *in* von Rad, U., Haq, B. U., and 26 others: Proceedings of the Ocean Drilling Program, Scientific results, Leg 122: College

Station Texas, Ocean Drilling Program, v. 122, p. 529–556, doi: 10. 2973/odp.proc.sr.122.149.1992.

Gardin, S., Galbrun, B., Thibault, N., Coccioni, R.,and Premoli Silva, I., 2012, Bio-magnetochronology for the upper Campanian-Maastrichtian from the Gubbio area, Italy: new results from the Contessa Highway and Bottaccione sections: Newsletters on Stratigraphy, v. 45, no. 1, p. 75–103, doi:10.1127/0078-0421/2012/0014.

Gayet, M., 2001, A review of some problems associated with the occurrences of fossil vertebrates in South America: Journal of South American Earth Sciences, v. 14, no. 2, p. 131–145.

Gough, D. O., 1981, Solar interior structure and luminosity variations. *in* Physics of Solar Variations, Springer, pp. 21–-34.

Gradstein, F.M., Ogg, J.G., Schmitz, M.D., and Ogg, G.M., 2012, The Geologic Time Scale 2012: Elsevier.

Hamilton, N., 1990, Mesozoic magnetostratigraphy of Maud Rise, Antarctica *in* Barker, P.F., Kennett, J.P., et al.: Proceedings of the Ocean Drilling Program, Scientific Results, Leg 113: College Station, TX (Ocean Drilling Program), v. 113, p. 255–260, doi:10.2973/odp.proc.sr.113.179.1990.

Hollister, C. D., Craddock, C, et al., 1976, Site 323: Initial Reports of the Deep Sea Drilling Project, Washington (U.S. Government Printing Office), v. 35, no. 4, p. 63–125, doi:10.2973/dsdp.proc.35.104.1976.

Huber, B.T., 1990, Maestrichtian planktonic foraminifer biostratigraphy of the Maud Rise (Weddell Sea, Antarctica): ODP Leg 113 Holes 689B and 690C *in* Barker, P.F., Kennett, J.P. et al.: Proceedings of the Ocean Drilling Program, Scientific Results, v. 113, p. 489–513, doi:10.2973/odp.proc.sr.113.135.1990.

Huber, B.T., MacLeod, K.G., and Tur, N.A., 2008, Chronostratigraphic framework for upper Campanian-Maastrichtian sediments on the Blake Nose (subtropical North Atlantic): Journal of Foraminiferal Research, v. 38, no. 2, p. 162–182.

Iturralde-Vinent, M.A., 2006, Meso-Cenozoic Caribbean paleogeography: implications for the historical biogeography of the region: International Geology Review, v. 48, no. 9, p. 791–827.

Iturralde-Vinent, M., and MacPhee, R.D., 1999, Paleogeography of the Caribbean region: implications for Cenozoic biogeography: Bulletin of the AMNH: no. 238.

Jung, C., Voigt, S., Friedrich, O., Koch, M.C., and Frank, M., 2013, Campanian–Maastrichtian ocean circulation in the tropical Pacific: Paleoceanography, v. 28, p. 562–573, doi:10.1002/palo.20051.

Lagabrielle, Y., Goddéris, Y., Donnadieu, Y., Malavieille, J., and Suarez, M., 2009, The tectonic history of Drake Passage and its possible impacts on global climate: Earth and Planetary Science Letters, v. 279, nos. 3–4, p. 197–211.

Lawver, L. A., Gahagan, L. M., and Coffin, M. F., 1992, The development of paleoseaways around Antarctica: The Antarctic Paleoenvironment: A Perspective on Global Change: Part One, p. 7–30.

Li, L., and Keller, G., 1999, Variability in Late Cretaceous climate and deep waters: evidence from stable isotopes: Marine Geology, v. 161, p. 171–190.

Lunt, D.J., et al., 2016, Palaeogeographic controls on climate and proxy interpretation: Climate of the Past, v. 12, no. 5, 1181–1198.

MacLeod, K.G., Huber, B.T., 1996, Reorganization of deep ocean circulation accompanying a Late Cretaceous extinction event: Nature, v. 380, p. 422–425.

MacLeod, K.G., and Bergen, J.A., 2004, Apparent cooling in the tropical Pacific during the Maastrichtian and diagenetic artifacts in Late Cretaceous stable isotopic trends in bulk carbonate from Ontong Java Plateau *in* Fitton, J.G., Mahoney, J.J., Wallace, P.J., and Saunders, A.D. (Eds.): Proceedings of the Ocean Drilling Program, Scientific Results, v. 192, p. 1–15, doi:10.2973/odp.proc.sr.192.108.2004.

MacLeod, K.G., Martin, E.E., and Blair, S.W., 2008, Nd isotopic excursion across the Cretaceous ocean anoxic event 2 (Cenomanian–Turonian) in the tropical North Atlantic: Geology, v. 36, no. 10, p. 811–814.

Macleod, K.G., Isaza Londoño, C., Martin, E.E., Jiménez Berrocoso, Á., and Basak, C., 2011, Changes in North Atlantic circulation at the end of the Cretaceous greenhouse interval: Nature Geoscience, v. 4, p. 779–782.

Mahoney, J.J., Fitton, J.G., Wallace, P.J., et al., 2001, Site 1186: Proceedings of the Ocean Drilling Program, Initial Reports, v. 192, no. 6, p. 1–117, doi:10.2973/odp.proc.ir.192.106.2001.

Markwick, P.J., and Valdes, P.J., 2004, Palaeo-digital elevation models for use as boundary conditions in coupled ocean–atmosphere GCM experiments: a Maastrichtian (late Cretaceous) example: Palaeogeography, Palaeoclimatology, Palaeoecology, v. 213, nos. 1–2, p. 37–63.

Moiroud, M., Pucéat, E., Donnadieu, Y., Bayon, G., Giraud, M., Voigt, S., Deconinck, J.F., and Monna, F., 2016, Evolution of neodymium isotopic signature of seawater during the Late Cretaceous: implications for intermediate and deep ocean circulation: Gondwana Research, v. 36, p. 503–522.

Murphy, D.P., and Thomas, D.J., 2012, Cretaceous deep-water formation in the Indian sector of the Southern Ocean: Paleoceanography, v. 27, p. PA1211, 1–12, doi:10.1029/2011PA002198.

Ortiz-Jaureguizar, E., and Pascual, R., 2011, The tectonic setting of the Caribbean region and the K/T turnover of the South American land-mammal fauna: Boletín Geológico y Minero, v. 122, no. 3, p. 333–344.

Pindell, J., Kennan, L., Stanek, K.P., Maresch, W., and Draper, G., 2006, Foundations of Gulf of Mexico and Caribbean evolution: eight controversies resolved: Geologica Acta, v. 4, nos. 1–2, p. 303–341.

Roth, P.H., 1981, Mid-Cretaceous calcareous nannoplankton from the central Pacific: Implications for paleoceanography: Initial Reports of the Deep Sea Drilling Project: Washington (U.S. Govt. Printing Office), v. 62, no. 13, p. 471–489, doi:10.2973/dsdp.proc.62.113.1981.

Sewall, J. O., Sloan, L. C., Huber, M., and Wing, S., 2000, Climate sensitivity to changes in land surface characteristics: Global and Planetary Change, v. 26, no. 4, p. 445–465.

Sewall, J. O., Van de Wal, R. S. W., Van Der Zwan, K., Van Oosterhout, C., Dijkstra, H. A., & Scotese, C. R., 2007, Climate model boundary conditions for four Cretaceous time slices, Climate of the Past, v. 3, no. 4, p. 647–657.

Schlanger, S.O., Jackson, E.D., et al., 1976, Site 317: Initial Reports of the Deep Sea Drilling Project: Washington (U.S. Govt. Printing Office), v. 33, no. 5, p. 161–300, doi:10.2973/dsdp.proc.33.105.1976.

Tabor, C.R., Poulsen, C.J., Lunt, D.J., Rosenbloom, N.A., Otto-Bliesner, B.L., Markwick, P.J., Brady, E.C., and Farnsworth, A., 2016, The cause of Late Cretaceous cooling: A multi-model/proxy comparison: Geology, v. 44, no. 11, p. 963–966, doi:10.1130/G38363.1.

Thiede, J., Valuer, T.L., et al., 1981, Site 463: Western Mid-Pacific Mountains: Initial Reports of the Deep Sea Drilling Project: Washington (U.S. Govt. Printing Office), v. 62, no. 2, p. 33–156, doi:10.2973/dsdp.proc.62.102.1981.

Thiede, J., and Rea, 1981, Site 464: Northern Hess Rise: Initial Reports of the Deep Sea Drilling Project: Washington (U.S. Govt. Printing Office), v. 62, no. 3, p. 157–197, doi:10.2973/dsdp.proc.62.103.1981.

Thomas, D.J., 2004, Evidence for deep-water production in the North Pacific during the early Cenozoic warm interval: Nature, v. 430, p. 65–68, doi:10.1038/nature02639.

Thomas, D.J., Korty, R., Huber, M., Schubert, J.A. and Haines, B., 2014, Nd isotopic structure of the Pacific Ocean 70–30 Ma and numerical evidence for vigorous ocean circulation and ocean heat transport in a greenhouse world: Paleoceanography, v. 29, p. 454–469, doi:10.1002/2013PA002535.

Vallier, T.L., Rea, D.K., et al., 1981, The geology of Hess Rise, central North Pacific Ocean: Initial Reports of the Deep Sea Drilling Project, v. 62, no. 61, p. 1031–1072, doi:10.2973/dsdp.proc.62.161.1981.

Vérard, C., Flores, K., and Stampfli, G., 2012, Geodynamic reconstructions of the South America–Antarctica plate system: Journal of Geodynamics, v. 53, p. 43–60.